Wave Propagation in Porous Piezoelectric Media

A. Chakraborty[1]

Abstract: A mathematical model is presented in this work that describes the behavior of porous piezoelectric materials subjected to mechanical load and electric field. The model combines Biot's theory of poroelasticity and the classical theory of piezoelectric material wherein it is assumed that piezoelectric coupling exists only with the solid phase of the porous medium. This model is used to analyze the stress and electric wave generated in bone and porous Lead-Zirconate-Titanate (PZT) due to high frequency pulse loading. The governing partial differential equations are solved in the frequency domain by transforming them into a polynomial eigenvalue structure. This approach permits an exact solution for elastic material properties. The material domain is assumed to be in the form of a layered medium where periodic boundary conditions are enforced in the longer direction. The frequency domain based formulation also helps in describing the frequency dependent material properties. The work presents analytical solutions for various essential and natural boundary conditions. The propagating nature of the elastic and electric wave in bone and porous PZT is investigated in detail. It is expected that this model will be instrumental in providing valuable insight into the mechanism of bone regeneration.

Keywords: Wave propagation, Bone, Porous ceramic, Biot's theory, Slow wave, Frequency domain

1   Introduction

A piezoelectric material is one which develops an electric charge when subjected to mechanical stress and conversely, generates mechanical stress when subjected to electric field. Naturally occurring piezoelectric materials were investigated in the 1880s, but piezoelectric ceramics and ferroelectricity were not discovered until the 1940s. Ceramics in the present day have moved from their original dense form to porous structures with applications in aerospace (radome material), automobile

[1] GM R&D, India Science Lab, Bangalore

(syntactic foam) and biomedical (as a bone-substitute) industries. A porous ceramic is akin to many natural substances like plants, soils, rocks, outcrops, even bone.

Bone is perhaps the most celebrated biological material that shows piezoelectric effect. Piezoelectricity in bone was discovered by Fukuda and Yasuda [1957] and their work was subsequently verified by other researchers [Bassett and Becker (1962), Shamos, Lavine, and Shamos (1963), McElhaney (1967), Anderson and Eriksson (1970), Marino and Becker (1970), Marino, Soderholm, and Becker (1971)]. This property has been used by researchers as an underlying mechanism to explain growth and resorption in bone [Gjelsavik (1973a,b)]. However, the possible physiological role of piezoelectricity has not been fully evaluated yet, because of limited modeling and experimental evidence. Studies of the dielectric and piezoelectric properties of bone, for example, raise the issue as to whether wet bone is piezoelectric at all physiological frequencies [Reinish (1975)]. It is found that piezoelectric effects occur in the kilo-hertz range, well above the range of physiologically significant frequencies [Reinish (1975)]. Further, both the dielectric and piezoelectric properties depend strongly upon the excitation frequency [Lakes and Katz (1977), Bur (1976)] with considerable magnitude of the imaginary part for d_{14} component [Bur (1976)]. Other than being piezoelectric it is also well-known that bone displays complex micro-structure with inhomogeneity, anisotropy and the presence of multiple phases, which require an averaging technique for efficient analysis of mechanical response. Biot's theory of poroelasticity [Biot (1955)] is a strong candidate among the different homogenization techniques and is used to explain bone response to ultrasonic excitation [Williams (1992)]. Thus, a realistic mathematical model of bone can be obtained by utilizing the poroelastic description coupled with piezoelectricity.

It is not surprising that porous piezo-ceramics find important applications as a bone-substitute. The scope of biomaterials for repairing bone defects has been broadened by the development of lead-free piezoelectric ceramics, such as alkaline niobate and barium titanate, due to their stable piezoelectricity and biocompatibility. Stress-generated potentials produced by piezoelectric ceramics may stimulate bone regeneration in situ [Braden, Bairstow, Beider, and Ritter (1966)], for example barium titanate implants may promote osteogenesis [Park, Kelly, Kenner, and Recum (1981)]. Porous implants are known to be more favorable than solid implants for osseointegration [Zhang, Li, and Zhang (2007)]. Porous bioceramics are also favorable because nutrient exchange is easier than in dense materials [Galassi (2006)].

The prediction of the response of either original bone or its implant substitute to mechanical loading or electric field remains challenging due to their unique material properties. Further, bone quality is often estimated by subjecting it to pulse

loading of very high frequency content and it becomes necessary to consider the frequency dependence of the elastic, dielectric and piezoelectric properties. However, the present literature is silent about a suitable mathematical model for porous piezoelectric materials and it is the author's belief that a confluence of Biot's theory of poroelasticity with the classical theory of piezoelectricity can provide a very good description of these materials.

This is attempted in the present work where Biot's theory of poroelasticity is enriched with a piezoelectric description of the material. Since porosity is one of the material parameters in Biot's theory, the current approach also enables us to accurately represent some of the porosity dependent piezoelectric material properties. The original governing equations of Biot's theory are augmented with the charge equation (Gauss's law) and are solved in the frequency domain (where they are converted into a set of ordinary differential equations that are solvable exactly). These exact solutions are used as interpolating polynomials, which leads to significant reduction in the cost of computation. Another advantage of this approach is that the frequency dependency of material properties can be described efficiently. Broadly falling under the method of integral transform, this methodology is called the spectral finite element method (SFEM) [Gopalakrishnan, Chakraborty, and RoyMahapatra (2007)], which has been used extensively in modeling two-dimensional inhomogeneous [Chakraborty and Gopalakrishnan (2004c, 2006a)] and anisotropic [Chakraborty and Gopalakrishnan (2004a)] layered media, anisotropic layer in the presence of nonclassical thermoelasticity [Chakraborty and Gopalakrishnan (2004b)], anisotropic plate [Chakraborty and Gopalakrishnan (2005, 2006b)] and inhomogeneous media with coupled piezoelasticity [Chakraborty, Gopalakrishnan, and Kausel (2005)]. Spectral elements have also been developed to describe the behavior of porous media with plane strain [Degrande and Roeck (1992)] and axisymmetric [Al-Khoury, Kasbergen, Scarpas, and Blaauwendraad (2002)] description. Recently the author has developed a poroelastic beam formulation with coupled axial-flexural motion for describing wave propagation behavior [Chakraborty (2009)].

Similar combined analytical-numerical approach is utilized in studying surface wave propagation in multi-layered piezoelectric plate [Han, Ding, and Liu (2005)]. Another variant of SFEM, called wavelet SFEM [Mitra and Gopalakrishnan (2006b)] is used successfully in modeling wave propagation behavior of carbon nanotube [Mitra and Gopalakrishnan (2008)], isotropic plate structure [Mitra and Gopalakrishnan (2006a)] and degraded composite beam [Tabrez, Mitra, and Gopalakrishnan (2007)]. Wave propagation behavior of homogeneous and isotropic media with and without piezoelectric effect is also studied by the method of Green's function [Wu and Chen (2007), Seyrafian, Gatmiri, and Noorzad (2006), Jabbari and Gatmiri

(2007), Dziatkiewicz and Fedelinski (2007)].

However, to the best of author's knowledge, there is no existing frequency domain formulation for coupled piezoelectric and poroelastic medium, as is carried out in this work. The next section describes the frequency domain element formulation, where the strong form of the governing partial differential equations for piezo-poro-elasticity is solved in the frequency-wavenumber domain and the unknown coefficients are computed by imposing Dirichlet and Neumann boundary conditions. Analytical expessions for the exact solutions for various loading and boundary conditions are also provided in this section. These formulations are subsequently utilized to capture the propagating slow and fast waves, characteristic of Biot's poroelastic theory. Further, the effect of piezoelectricity on the elastic waves and the nature of the electric pulse propagation are investigated for a bone material with low piezoelectric effect and for a porous piezoelectric material with substantial piezoelectric effect. Conclusions from these exercises and the scope for future work are provided in the last section.

2   Mathematical Model

It is assumed that displacements are small, the material is isotropic and porous with solid and fluid phase (as described by Biot) and the domain is two-dimensional (2D) Euclidean space. The governing equations in the presence of coupled piezoelectric effects are obtained by augmenting the original equations of Biot with the charge equation (Gauss's law) and written in the indicial notation (with summation over the repeated indices) as

$$
\begin{aligned}
\sigma_{ij,j} &= \rho_{11}\ddot{u}_i + \rho_{12}\ddot{U}_i + b(\dot{u}_i - \dot{U}_i), \\
s_{,i} &= \rho_{12}\ddot{u}_i + \rho_{22}\ddot{U}_i - b(\dot{u}_i - \dot{U}_i), \\
D_{i,i} &= 0,
\end{aligned}
\tag{1}
$$

where σ_{ij} and s are the solid and fluid stress components, respectively, ρ_{11}, ρ_{12} and ρ_{22} are Biot's inertial parameters, b is the viscous damping coefficient and D_i is the component of the electric displacement. The motion of the medium is described by the solid (u_i) and fluid (U_i) displacement fields. Further, a comma in the subscript denotes differentiation with respect to the spatial variable after the comma and over-dot denotes differentiation with respect to time, t. The stresses and electric displacement are related to the solid and fluid strains by the extended

constitutive law

$$
\begin{aligned}
\sigma_{ij} &= 2NS_{ij} + (AS_{kk} + Q\theta)\delta_{ij} - e_{kij}E_k, \\
s &= QS_{kk} + R\theta, \\
D_k &= e_{kij}S_{ij} + \varepsilon_{ki}E_i,
\end{aligned}
\tag{2}
$$

where A, N, Q and R are Biot's elastic parameters and e_{kij} and ε_{ij} are the piezo-electric constants and dielectric constants, respectively. The solid strains S_{ij}, fluid strain θ and the electric field E_i are related to the displacement components and electric potential ϕ by

$$
S_{ij} = (u_{i,j} + u_{j,i})/2, \quad \theta = U_{i,i}, \quad E_i = -\phi_{,i}.
\tag{3}
$$

Limiting the domain of interest to the $x_1 - x_3$ plane and writing x for x_1 and z for x_3, the general stress-strain relation becomes

$$
\begin{Bmatrix}
\sigma_{xx} \\
\sigma_{zz} \\
\sigma_{xz} \\
s \\
D_x \\
D_z
\end{Bmatrix}
=
\begin{bmatrix}
A+2N & A & 0 & Q & 0 & -e_{31} \\
A & A+2N & 0 & Q & 0 & -e_{33} \\
0 & 0 & N & 0 & -e_{15} & 0 \\
Q & Q & 0 & R & 0 & 0 \\
0 & 0 & e_{15} & 0 & \varepsilon_{11} & 0 \\
e_{31} & e_{33} & 0 & 0 & 0 & \varepsilon_{33}
\end{bmatrix}
\begin{Bmatrix}
S_{xx} = u_{x,x} \\
S_{zz} = u_{z,z} \\
2S_{xz} = u_{x,z} + u_{z,x} \\
\theta = U_{x,x} + U_{z,z} \\
E_x = -\phi_{,x} \\
E_z = -\phi_{,z}
\end{Bmatrix},
\tag{4}
$$

which on substitution in Eq. 1 generates the five governing equations as

$$
\begin{aligned}
Pu_{x,xx} + Nu_{x,zz} + (A+N)u_{z,xz} \;+\;& Q(U_{x,xx} + U_{z,xz}) + (e_{31} + e_{15})\phi_{xz} \\
=\;& \rho_{11}\ddot{u}_x + \rho_{12}\ddot{U}_x + b(\dot{u}_x - \dot{U}_x),
\end{aligned}
\tag{5}
$$

$$
\begin{aligned}
Nu_{z,xx} + Pu_{z,zz} + (A+N)u_{x,xz} \;+\;& Q(U_{x,xz} + U_{z,zz}) + e_{15}\phi_{xx} + e_{33}\phi_{zz} \\
=\;& \rho_{11}\ddot{u}_z + \rho_{12}\ddot{U}_z + b(\dot{u}_z - \dot{U}_z),
\end{aligned}
\tag{6}
$$

$$
Q(u_{x,xx} + u_{z,xz}) + R(U_{x,xx} + U_{z,xz}) = \rho_{12}\ddot{u}_x + \rho_{22}\ddot{U}_x - b(\dot{u}_x - \dot{U}_x),
\tag{7}
$$

$$
Q(u_{x,xz} + u_{z,zz}) + R(U_{x,xz} + U_{z,zz}) = \rho_{12}\ddot{u}_z + \rho_{22}\ddot{U}_z - b(\dot{u}_z - \dot{U}_z),
\tag{8}
$$

$$
(e_{31} + e_{15})u_{x,xz} + e_{15}u_{z,xx} + e_{33}u_{z,zz} - \varepsilon_{11}\phi_{,xx} - \varepsilon_{33}\phi_{,zz} = 0,
\tag{9}
$$

where $P = A + 2N$. To solve these equations, the solutions of the unknown displacements and potentials are assumed as a superposition of harmonics in time and

space (x direction) as

$$
\left\{
\begin{array}{c}
u_x(x,z,t)\\
u_z(x,z,t)\\
U_x(x,z,t)\\
U_z(x,z,t)\\
\phi(x,z,t)
\end{array}
\right\}
=\sum_{m=1}^{M}\sum_{n=1}^{N}
\left\{
\begin{array}{c}
u_{x0}(z)\sin(\eta_m x)\\
u_{z0}(z)\cos(\eta_m x)\\
U_{x0}(z)\sin(\eta_m x)\\
U_{z0}(z)\cos(\eta_m x)\\
\phi_{x0}(z)\cos(\eta_m x)
\end{array}
\right\}e^{-I\omega_n t},\quad I^2=-1,
\tag{10}
$$

where ω_n is the discrete circular frequency and η_m is the wavenumber in x direction. Substituting the above assumed solution into Eqs. 5–9, a set of ordinary differential equations (ODEs) is obtained in the variable z. As these equations have constant coefficients, their solution is of the form of $A\exp(-Ikz)$, where k is the wavenumber in the z direction. Substituting this form in the ODEs, the algebraic form of the governing equations are obtained as

$$
\Psi(k)\tilde{u}=\big(\mathbf{A_0}(\eta_m,\omega_n)+k\mathbf{A_1}(\eta_m,\omega_n)+k^2\mathbf{A_2}(\eta_m,\omega_n)\big)\tilde{u}=\mathbf{0},
\tag{11}
$$

which is a quadratic eigenvalue problem (QEP) for the unknown eigenvector $\tilde{u}$ and eigenvalue k. The submatrices are (with $M_{ij}=\rho_{ij}-(-1)^{i+j}Ib/\omega$)

$$
\mathbf{A_0}=\left[
\begin{array}{ccccc}
-P\eta^2+\omega^2 M_{11} & 0 & -Q\eta^2+M_{12}\omega^2 & 0 & 0\\
0 & -N\eta^2+\omega^2 M_{11} & 0 & \omega^2 M_{12} & -e_{15}\eta^2\\
-Q\eta^2+\omega^2 M_{12} & 0 & -R\eta^2+\omega^2 M_{22} & 0 & 0\\
0 & \omega^2 M_{12} & 0 & \omega^2 M_{22} & 0\\
0 & -e_{15}\eta^2 & 0 & 0 & \varepsilon_{11}\eta^2
\end{array}
\right],
\tag{12}
$$

$$
\mathbf{A_1}=\left[
\begin{array}{ccccc}
0 & I(A+N)\eta & 0 & IQ\eta & I(e_{15}+e_{31})\eta\\
-I(A+N)\eta & 0 & -IQ\eta & 0 & 0\\
0 & IQ\eta & 0 & IR\eta & 0\\
-IQ\eta & 0 & -IR\eta & 0 & 0\\
-I(e_{15}+e_{31})\eta & 0 & 0 & 0 & 0
\end{array}
\right],
\tag{13}
$$

$$
\mathbf{A_2}=\left[
\begin{array}{ccccc}
-N & 0 & 0 & 0 & 0\\
0 & -P & 0 & -Q & -e_{33}\\
0 & 0 & 0 & 0 & 0\\
0 & -Q & 0 & -R & 0\\
0 & -e_{33} & 0 & 0 & \varepsilon_{33}
\end{array}
\right],
\tag{14}
$$

where it is evident that for $\eta = 0$, $\mathbf{A_1} \equiv 0$ and $\mathbf{A_0}$ is singular, whereas $\mathbf{A_2}$ is singular for all η. Thus, the QEP has infinite eigenvalues (wavenumbers) and looking at the rank of $\mathbf{A_2}$ it can be said that there will be eight finite eigenvalues for $\eta \neq 0$. These values are obtained from the condition that for nontrivial solutions of $\tilde{u}$, the determinant of the Lambda matrix $\Psi(k)$ must be zero. The resulting spectrum relation for k is

$$C_1 k^8 + C_2 k^6 + C_3 k^4 + C_4 k^2 + C_5 = 0, \quad C_i = C_i(\omega_n, \eta_m \neq 0). \tag{15}$$

For $\eta = 0$, C_1 is zero and the number of nonzero k is reduced to six. The number of independent unknowns is also reduced to three as

$$\phi_0(z) = (e_{33}/\varepsilon_{33})u_{z0}(z), \quad U_{x0}(z) = (-M_{12}/M_{22})u_{x0}(z). \tag{16}$$

For the general case of $\eta \neq 0$, the solutions of the ODEs are written as

$$\left\{ \begin{array}{c} u_{x0}(z) \\ u_{z0}(z) \\ U_{x0}(z) \\ U_{z0}(z) \\ \phi_0(z) \end{array} \right\} = \sum_{i=1}^{8} A_i \left\{ \begin{array}{c} R_{1i} \\ R_{2i} \\ R_{3i} \\ R_{4i} \\ R_{5i} \end{array} \right\} \exp(-Ik_i z), \tag{17}$$

where A_i are the unknown coefficients to be determined from the boundary conditions. The elements of the matrix $\mathbf{R}$ can be obtained from the eigenvectors of Ψ. An alternate approach of obtaining $\mathbf{R}$ stems from the fact that for wavenumber k_i, the i-th column $\mathbf{R}$ (written as $R(:,i)$) satisfies the relation $\Psi(k_i)R(:,i) = \mathbf{0}$. Thus, the columns of $\mathbf{R}$ lie in the null space of Ψ. Using the singular value decomposition of $\Psi(k_i)$ (note that $\Psi(k_i)$ is singular for each k_i and thus admits atleast one non-trivial null space element) $R(:,i)$ is obtained.

The boundary conditions are in terms of the components of tractions T_x and T_z in the solid phase, pressure s in the fluid phase and resultant electric displacement D. These quantities are related to the solid stress and electric displacement components by

$$T_x = \sigma_{xx} n_x + \sigma_{xz} n_z, \quad T_z = \sigma_{xz} n_x + \sigma_{zz} n_z, \quad D = D_x n_x + D_z n_z, \tag{18}$$

where the first two relations are coming from Cauchy's principle and n_x and n_z are the components of the surface normal in the x and z direction, respectively. In the present case, the boundaries of the domain are assumed parallel to the x axis, *i.e.*, $n_x = 0$ and $n_z = \mp 1$. Altogether, there are four natural boundary conditions at each edge. However, there are five displacement boundary conditions, *i.e.*, two solid displacements, two fluid displacements and the electric potential, resulting in an

under-determinate system. Since a fluid element cannot support an applied shear stress, we neglect the x component of the fluid displacement (U_x), and retain the rest as unknowns (three displacement components and the potential).

One advantage of the frequency domain formulation is that the solution is constructed as a (complete) linear combination of the wavenumber components. Thus, we have the choice of considering only the forward moving components, which represent an infinite layer, or, we can consider all the wavenumber components, which will describe the behavior of a semi-infinite layer. First, we present a description of the half-space and next for a semi-infinite layer.

2.1   Formulation for a half-space

In this case, only the forward moving wavenumbers are considered and the solutions of the unknowns are written as

$$
\left\{
\begin{array}{c}
u_{x0}(z) \\
u_{z0}(z) \\
U_{z0}(z) \\
\phi_0(z)
\end{array}
\right\}
= \sum_{i=1}^{4} A_i
\left\{
\begin{array}{c}
R_{1i} \\
R_{2i} \\
R_{4i} \\
R_{5i}
\end{array}
\right\}
\exp(-Ik_i z).
\tag{19}
$$

Evaluating Eq. 19 at $z = 0$ and identifying the unknowns as the edge variables $\mathbf{v}_1 = \{u_{x1}, u_{z1}, U_{z1}, \phi_1\}$, a relation is established between $\mathbf{v}_1$ and the coefficients A_i as

$$
\mathbf{v}_1 = \mathbf{T}_1 \mathbf{a}^+, \quad \mathbf{a}^+ = \{A_1, A_2, A_3, A_4\},
\tag{20}
$$

where $\mathbf{T}_1$ consists of suitable rows of $\mathbf{R}$ and can be thought as the matrix of coordinate transformation between the canonical coordinate system in the frequency-wavenumber domain and the physical coordinate system.

From Eq. 18, the natural boundary condition at $z = 0$ ($n_z = -1$) can be written as

$$
\mathbf{f}_1 = \{-\sigma_{xz}, -\sigma_{zz}, -s, -D_z\}_{z=0}^{T},
\tag{21}
$$

where T in the superscript denotes transpose of a vector/matrix. Using Eq. 4 and 19, $\mathbf{f}_1$ can be expressed in terms of the unknown coefficients A_i as

$$
\mathbf{f}_1 = \mathbf{T}_2 \mathbf{a}^+,
\tag{22}
$$

which together with Eq. 20 relates to the unknown edge displacements and potential as

$$
\mathbf{f}_1 = \mathbf{T}_2 \mathbf{T}_1^{-1} \mathbf{v}_1 = \mathbf{K} \mathbf{v}_1,
\tag{23}
$$

where $\mathbf{K}$ serves as a stiffness matrix (4×4) of the half-space at frequency ω and horizontal wavenumber η. As the formulation is based on the exact solution in the transformed domain the matrix $\mathbf{K}$ can be thought as an exact representation of a half-space.

2.2 Formulation for a semi-infinite layer

For a semi-infinite layer, there are two edges where boundary conditions are to be prescribed. The solutions are considered to be a complete linear combination of both the forward and backward moving components as given in Eq. 17. Following the same procedure as outlined before, Eq. 17 is evaluated at $z = 0$ and $z = L$ (L is the thickness of the layer) to obtain a relation between the edge displacements and potentials and the unknown coefficients as

$$\mathbf{v} = \{\mathbf{v}_1, \mathbf{v}_2\}^T = \mathbf{T}_1 \mathbf{a}, \quad \mathbf{a} = \{\mathbf{a}^+, \mathbf{a}^-\}^T = \{A_1, \dots, A_8\}, \tag{24}$$

where $\mathbf{v}_2$ is the vector of unknowns at $z = L$. Similarly, the natural boundary conditions at $z = L, (n_z = +1)$ can be written as

$$\mathbf{f}_2 = \{\sigma_{xz}, \sigma_{zz}, s, D_z\}^T_{z=L}, \tag{25}$$

which together with Eqs. 21 and 17 relates the natural boundary conditions to the unknown coefficients as

$$\mathbf{f} = \{\mathbf{f}_1, \mathbf{f}_2\}^T = \mathbf{T}_2 \mathbf{a}. \tag{26}$$

Substituting Eq. 24 in Eq. 26 the stiffness matrix (8×8) of a layer is obtained which is of the same form as given in Eq. 23. It is worth noting that this form is quite generalized and is not particular to any set of boundary conditions. Thus, different solutions for different boundary conditions can be obtained from this single equation.

Equation 23 represents a layer at frequency ω_n and wavenumber η_m. To obtain the complete solutions, this equation needs to be solved $M \times N$ times. The discrete values of the horizontal wavenumber, η_m is related to x_1-window length X_L and M by

$$\eta_m = 2\pi(m-1)/X_L = 2\pi(m-1)/M\Delta x_1. \tag{27}$$

The window length is dictated by the geometry of the structure to be analyzed and M is dictated by the spatial variation of the applied stress in x_1 direction.

It is to be noted that the present form of the representation of a layer can easily be modified to the form of propagator matrix. To achieve this, the essential and natural

boundary conditions of one edge are related to their counterparts of the other edge as

$$\left\{ \begin{array}{c} \mathbf{f}_1 \\ \mathbf{v}_1 \end{array} \right\} = \left[\begin{array}{cc} \mathbf{P}_{11} & \mathbf{P}_{12} \\ \mathbf{P}_{21} & \mathbf{P}_{22} \end{array} \right] \left\{ \begin{array}{c} \mathbf{f}_2 \\ \mathbf{v}_2 \end{array} \right\}, \tag{28}$$

where $\mathbf{P}_{ij}$ are the submatrices of the propagator matrix $\mathbf{P}$. These matrices can be written in terms of the submatrices of $\mathbf{K}$ as

$$\mathbf{P}_{11} = \mathbf{K}_{11}\mathbf{K}_{21}^{-1}, \mathbf{P}_{12} = \mathbf{K}_{11}\mathbf{K}_{21}^{-1}\mathbf{K}_{22} + \mathbf{K}_{12}, \mathbf{P}_{21} = \mathbf{K}_{21}^{-1}, \mathbf{P}_{22} = -\mathbf{K}_{21}^{-1}\mathbf{K}_{22}, \tag{29}$$

where $\mathbf{K}$ is partitioned in the same way as done for $\mathbf{P}$.

3 Reduction to 1D Case

Although the solution of Eq. 15 provides a complete picture of the propagating modes in a porous piezoelectric media, much insight can be gained by studying the propagation of these waves in a one-dimensional system, which will also be helpful in deriving closed form solutions of the phase speed. Considering the propagation of bulk wave in the z direction, the unknown variables are the solid (u_z) and fluid (U_z) displacement components and potential ϕ, which are related to the relevant stresses and electric displacement by

$$\begin{array}{rcl} \sigma_{zz} & = & Pu_{z,z} + QU_{z,z} + e_{33}\phi_{,z} \\ s & = & Qu_{z,z} + RU_{z,z} \\ D_z & = & e_{33}u_{z,z} - \varepsilon_{33}\phi_{,z}. \end{array} \tag{30}$$

The governing equations are simplified to

$$\begin{array}{rcl} Pu_{z,zz} + QU_{z,zz} + e_{33}\phi_{,zz} & = & \rho_{11}\ddot{u}_z + \rho_{12}\ddot{U}_z + b(\dot{u}_z - \dot{U}_z), \\ Qu_{z,zz} + RU_{z,zz} & = & \rho_{12}\ddot{u}_z + \rho_{22}\ddot{U}_z - b(\dot{u}_z - \dot{U}_z), \\ e_{33}u_{z,zz} - \varepsilon_{33}\phi_{,zz} & = & 0. \end{array} \tag{31}$$

Utilizing the third equation, the first one is modified to

$$(P + e_{33}^2/\varepsilon_{33})u_{z,zz} + QU_{z,zz} = \rho_{11}\ddot{u}_z + \rho_{12}\ddot{U}_z + b(\dot{u}_z - \dot{U}_z), \tag{32}$$

which together with the second of Eq. 31 describe the motion of the solid and fluid in z direction. Assuming the general form of the solution as

$$u_z(z,t) = u_0 e^{I(\omega t - kz)}, \quad U_z(z,t) = U_0 e^{I(\omega t - kz)}, \tag{33}$$

and substituting in the governing equations, the algebraic eigenvalue problem becomes

$$
\begin{bmatrix} \omega^2 M_{11} - k^2 \bar{P}, & \omega^2 M_{12} - k^2 Q \\ \omega^2 M_{12} - k^2 Q, & \omega^2 M_{22} - k^2 R \end{bmatrix} \begin{Bmatrix} u_\circ \\ U_\circ \end{Bmatrix} = \begin{Bmatrix} 0 \\ 0 \end{Bmatrix},
\tag{34}
$$

where $\bar{P} = P + e_{33}^2/\varepsilon_{33}$ and M_{ij} is as defined before. Following the same argument of nontrivial solution for $u_\circ$ and $U_\circ$, the characteristic equation for k is obtained, which is a quartic equation in standard form compared to the polynomial of degree eight in Eq. 15. Rewriting the characteristic equation as

$$
a_\circ k^4 + b_\circ k^2 \omega^2 + c_\circ \omega^4 = 0,
\tag{35}
$$

the roots become

$$
k^2 = \omega^2 \left(\frac{-b_\circ \pm \sqrt{b_\circ^2 - 4 a_\circ c_\circ}}{2 a_\circ} \right).
\tag{36}
$$

As the phase speed is defined as $V = \omega/\mathrm{Re}(k)$, the expressions for the fast and slow phase speeds are readily obtained as

$$
V_{1,2} = \mathrm{Re} \left[\left(\frac{2 a_\circ}{-b_\circ \pm \sqrt{b_\circ^2 - 4 a_\circ c_\circ}} \right)^{1/2} \right],
\tag{37}
$$

where Re( ) denotes the real part of a complex number. Similarly, the imaginary part of the roots of Eq. 36 provides the attenuation, which can be written explicitly for the fast and slow waves as

$$
\mathscr{A}_{1,2} = \mathrm{Im} \left[\left(\frac{-b_\circ \pm \sqrt{b_\circ^2 - 4 a_\circ c_\circ}}{2 a_\circ} \right)^{1/2} \right] \omega,
\tag{38}
$$

where Im( ) indicates the imaginary part of a complex number. It is to be noted that the wavenumbers become complex quantities due to the introduction of dynamic tortuosity Johnson, Koplik, and Dashen (1987).

3.1 Solution for a semi-infinite layer

The complete solution of the displacement field at frequency ω is

$$
u_z(z, \omega) = \sum_{i=1}^{4} R_{1i} A_i(\omega) e^{-I k_i z}, \quad U_z(z, \omega) = \sum_{i=1}^{4} R_{2i} A_i(\omega) e^{-I k_i z},
\tag{39}
$$

where the columns of $\mathbf{R}$ satisfy Eq. 34. Integrating the last relation in Eq. 31,

$$\phi(z,\omega) = \alpha u_z(z,\omega) + A_5(\omega)z + A_6(\omega), \quad \alpha = e_{33}/\varepsilon_{33}, \tag{40}$$

where A_5 and A_6 are the constants of integration. The constitutive relations are modified to

$$
\begin{aligned}
\sigma_{zz} &= \bar{P}u_{z,z} + QU_{z,z} + e_{33}A_5, \\
s &= Qu_{z,z} + RU_{z,z}, \\
D_z &= -\varepsilon_{33}A_5, \forall z \in [0,L].
\end{aligned}
\tag{41}
$$

Thus, the electric displacement becomes independent of solid/fluid displacement components (hence independent of z), *i.e.*, constant in the entire layer. Since, the coefficient A_6 is not involved in the definitions of the stress/electric displacement, this coefficient can not be determined. The electric boundary condition can be either, (a) charge free (open circuit) *i.e.*, $D_z = 0$ at $z = 0, L$ or (b) nonzero applied charge density, $D_z = \bar{D}$ at $z = 0, L$. Further, the specified value of D_z at the boundary becomes its value for the entire layer. In the first case, $D_z = 0$ implies $A_5 = 0$ and $-\phi_z = E_z = -\alpha u_z$. For case (b), A_5 can be expressed in terms of $\bar{D}$ as $A_5(\omega) = -\bar{D}(\omega)/\varepsilon_{33}$ and the normal stress is modified as

$$\sigma_{zz} = \bar{P}u_{z,z} + QU_{z,z} - \alpha\bar{D} \tag{42}$$

Using the displacement solutions given in Eq. 39 in the reduced constitutive relations, the stresses are related to the unknown constants $\{A_1,\ldots,A_4\}$. The force vector comprises of the normal stress (σ_{zz}) and fluid pressure (s) as

$$\mathbf{f} = \{-\sigma_{zz}(0), -s(0), \sigma_{zz}(L), s(L)\} = \mathbf{T}_2\mathbf{a} + \alpha\bar{D}\mathbf{1}_-^+, \quad \mathbf{1}_-^+ = \{1,0,-1,0\}^T, \tag{43}$$

where the elements of the matrix $\mathbf{T}_2$ are

$$
\begin{aligned}
T_2(1,i) &= Ik_i(\bar{P}R_{1i} + QR_{2i}), \quad T_2(2,i) = Ik_i(QR_{1i} + RR_{2i}), \\
T_2(3,i) &= -T_2(1,i)\exp(-Ik_iL), T_2(4,i) = -T_2(2,i)\exp(-Ik_iL),
\end{aligned}
\tag{44}
$$

where i ranges from 1 to 4. The coefficients $A_1,\ldots,A_4$ are related to the nodal displacements at $z = 0$ (u_1, U_1) and $z = L$ (u_2, U_2) by

$$\mathbf{u} = \{u_1, U_1, u_2, U_2\}^T = \mathbf{T}_1\{A_1, A_2, A_3, A_4\}^T = \mathbf{T}_1\mathbf{a}, \tag{45}$$

where $\mathbf{T}_1$ is

$$\mathbf{T}_1 = \begin{bmatrix} R_{11} & R_{12} & R_{13} & R_{14} \\ R_{21} & R_{22} & R_{23} & R_{24} \\ R_{11}e_1 & R_{12}e_2 & R_{13}e_3 & R_{14}e_4 \\ R_{21}e_1 & R_{22}e_2 & R_{23}e_3 & R_{24}e_4 \end{bmatrix}, e_i = \exp(-Ik_iL). \tag{46}$$

Combining Eqs. 43 and 45 the equilibrium equation at frequency ω is

$$\mathbf{f} = \mathbf{T_2 T_1}^{-1}\mathbf{u} + \alpha \bar{D}\mathbf{1}_-^+ = \mathbf{K}\mathbf{u} + \alpha \bar{D}\mathbf{1}_-^+, \tag{47}$$

where $\mathbf{K}$ is the stiffness matrix of a layer.

3.2 Solution for a half-space

Considering only the forward propagating waves the solutions are

$$
\begin{aligned}
u_z(z) &= R_{11}A_1 \exp(-Ik_1 z) + R_{12}A_2 \exp(-Ik_2 z), \\
U_z(z) &= R_{21}A_1 \exp(-Ik_1 z) + R_{22}A_2 \exp(-Ik_2 z), \\
\phi_z(z) &= -I\alpha\left(k_1 R_{11}A_1 \exp(-Ik_1 z) + k_2 R_{12}A_2 \exp(-Ik_2 z)\right) + A_5.
\end{aligned} \tag{48}
$$

Evaluating these expressions at $z = 0$ the edge displacements and potential can be written in terms of the unknown coefficients as

$$
\mathbf{u_1} = \left\{ \begin{array}{c} u_z(0) = u_1 \\ U_z(0) = U_1 \\ \phi_z(0) = -E_1 \end{array} \right\} = \left[\begin{array}{ccc} R_{11} & R_{12} & 0 \\ R_{21} & R_{22} & 0 \\ -I\alpha k_1 R_{11} & -I\alpha k_2 R_{12} & 1 \end{array} \right] \left\{ \begin{array}{c} A_1 \\ A_2 \\ A_5 \end{array} \right\} = \mathbf{T_1 a}. \tag{49}
$$

Similarly, the stresses and electric displacement at $z = 0$ can be written in terms of $\mathbf{a}$ as

$$
\mathbf{f_1} = \left\{ \begin{array}{c} -\sigma_{zz}(0) \\ -s(0) \\ -D_z(0) \end{array} \right\} = \left[\begin{array}{ccc} Ik_1(\bar{P}R_{11} + QR_{21}) & Ik_2(\bar{P}R_{12} + QR_{22}) & -e_{33} \\ Ik_1(QR_{11} + RR_{21}) & Ik_2(QR_{12} + RR_{22}) & 0 \\ 0 & 0 & \varepsilon_{33} \end{array} \right] \mathbf{a} = \mathbf{T_2 a}. \tag{50}
$$

The stiffness matrix for the half-space then can be written in terms of matrices $\mathbf{T_2}$ and $\mathbf{T_1}$ as $\mathbf{K} = \mathbf{T_2 T_1}^{-1}$. In this case, we have the flexibility to study both open-circuit ($D_z = 0$) and short-circuit ($\phi = 0$) boundary conditions.

4 Numerical Examples

The developed frequency domain solutions are first verified by comparing their responses with the commercial FE code LS-DYNA based predictions in time domain. For this exercise, the material properties of bone are considered, where very low coupling exists between the electric and elastic parameters. Next, the same bone sample is subjected to electric pulse and both mechanical and electric field variables are measured. To show the effect of higher electro-elastic coupling a porous PZT sample is considered next and subjected to both mechanical loading and electric field. The variables of interest (*i.e.*, stress, strain, electric potential, *etc.*) are measured and compared with the responses of the bone material.

Parameter	Value	Parameter	Value
E_s	20.0 GPa	ν_s	0.32
ρ_s	1960 kg/m^3	ν_b	0.32
ρ_f	930 kg/m^3	n	1.32
K_f	2.2 GPa	τ	0.25
Λ	5.0×10^{-6} m	μ	1.0×10^{-3} Ns/m^2
e_{31}	1.51×10^{-3} C/m^2	e_{33}	1.87×10^{-3} C/m^2
e_{15}	3.58×10^{-3} C/m^2		
ε_{11}	88.54×10^{-12} F/m	ε_{33}	106.25×10^{-12} F/m

Table 1: Material properties of cortical bone considered in this study, piezoelectric properties are taken from Fotiadis, Foutsitzi, and Massalas (1999)

4.1   *Response of bone to mechanical loading and electric field*

First, we simulate the propagation of fast and slow waves through bone modeled as a layered medium. The force history considered is a single sinusoid multiplied by Hamming window (shown in Fig. 1)

$$f(t) = F_\circ \sin(2\pi f_\circ t)[0.54 - 0.46\cos(2\pi f_\circ t)], 0 \leq t \leq 1/f_\circ, \tag{51}$$

where $F_\circ$ is a constant (taken unity in this case) and $f_\circ$ is the center frequency which is taken as 0.75 MHz. The function is represented by a time sampling rate of 1.0×10^{-9} s with the number of frequency points, $N = 2^{16}$. Thus, the corresponding frequency sampling rate is 15.26 kHz and the Nyquist frequency is 500 MHz. However, as the load is band limited between 0 and 5 MHz (as shown in the inset of Fig. 1), for frequencies higher than 5 MHz the solution can be assumed to be zero. This realization considerably reduces the cost of computation.

The load is applied at one edge of a cortical bone of 9 mm thickness whose other edge is constrained. For 2D approximation, the load is assumed to vary according to a Gaussian function, $S(x) = \exp[\log(10^{-6}x^2/a^2)]$ with $a = 0.1$ m, which is symmetric about $X = 0$ (as shown in the inset of Fig. 2). Again, in this case, the present spatial variation is band limited, *i.e.*, the Fourier cosine coefficients (a_m) are negligible beyond a certain number. As Fig. 2 suggests all a_m for $m \geq 100$ can be neglected and for all subsequent simulations, M (as defined in Eq. 27) is fixed at 100. The material properties of the bone are described in Table 1. The FE model analysed in LS-DYNA has homogeneous material properties (there is no existing porous material in LS-DYNA model) with Young's modulus of 20 GPa, $\nu = 0.32$ and density of solid $\rho_s = 1960$ kg/m^3. For these material parameters, the wave
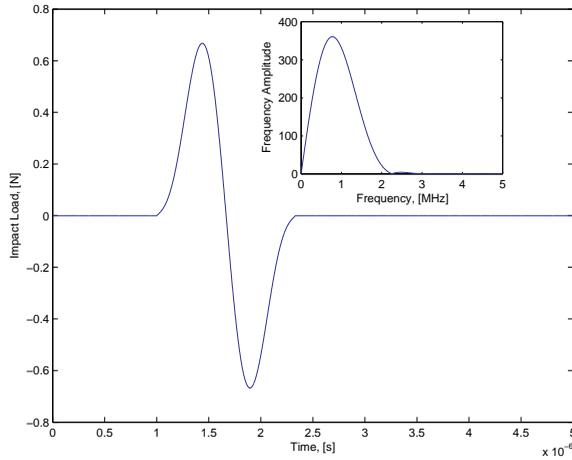
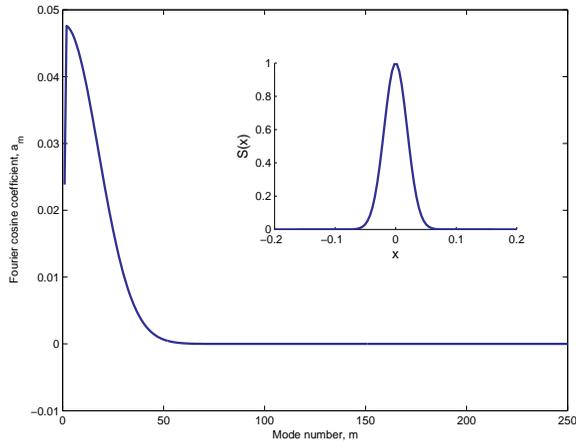Figure 1: Applied high frequency loading as defined by Eq. 51 (the inset shows frequency domain representation)

Figure 2: Fourier cosine coefficients of the applied load (the inset shows the spatial distribution)
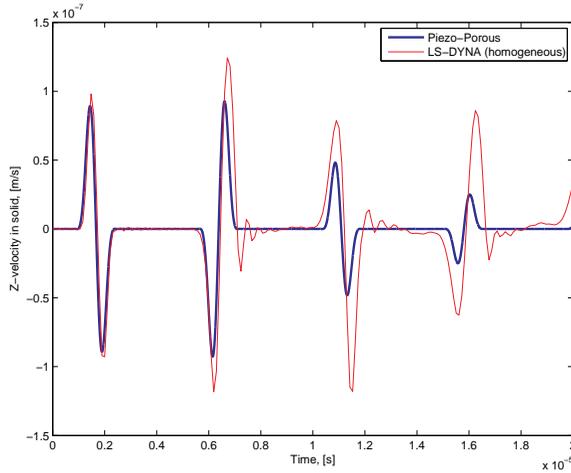
Figure 3: Surface *z*-velocity history in solid as predicted by the present method and LS-DYNA solutions, 0% porosity

speed for P-wave given by

$$C_p = \sqrt{\frac{E_s(1-v_s)}{\rho_s(1+v_s)(1-2v_s)}} \tag{52}$$

is 3821.23 m/s. Taking the maximum frequency content of the excitation as 2 MHz (see inset of Fig. 1), the minimum wavelength involved is of the order of $(3821.23 \times 10^3)/(2\pi \times 2 \times 10^6) = 0.3$ mm. For accurate prediction by FE, the element size should be of the order of the wavelength (or lesser). However, keeping in mind the cost of computation involved, we restrict the element size to 0.5 mm. Thus, for our model of dimension 1000 ×9 mm in *X* and *Z* direction, respectively, the FE model has 36000 shell elements in plane-strain condition.

The load is applied in the *Z* (thickness) direction and the velocity of solid material in the same direction is measured at the point of application of the load. First, we consider a porosity of 0.001 to minimize the effect of fluid present in the porous bone. The velocity histories for this case are plotted in Fig. 3. In this figure, the waveform at 1 μs is the incident wave and the following waveforms at around 6, 11 and 15 μs are reflections from the fixed end. The present solution and FE response agree closely with each other. However, the phase speed predicted by Eq. 37 for a porosity of 0.001 is 3820.03 m/s. The small difference in the magnitude of the phase speed computed from Eq. 52 and Eq. 37 causes the FE reflections to arrive earlier than the porous wave solution. This difference is more pronounced for
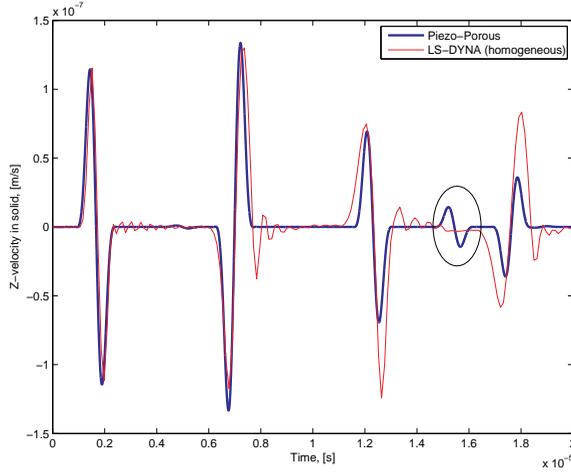
Figure 4: Surface *z*-velocity history in solid as predicted by the present method and LS-DYNA solutions for 50% porosity, the ellipse encloses the slow wave mode

the second and third reflection. It is evident that, to make the wave speed of the homogeneous medium comparable to that of porous medium, the Young's modulus should be decreased. An estimation of the reduced Young's modulus can be obtained by equating the wave speed for porous media to the wave speed of the P-wave and solving for E_s as

$$E_s = V_f^2 \frac{\rho_s (1 + v_s)(1 - 2v_s)}{(1 - v_s)}, \tag{53}$$

where V_f is the speed of the fast wave. Thus, for a porosity of 50 %, where $V_f = 3380$ m/s, the equivalent Young's modulus will be 15.67 GPa. Using this value of Young's modulus for the FE model, the *Z*-velocity is obtained for the previous load and plotted in Fig. 4 along with the porous media solution. It is evident that the frequency domain based porous media solution agrees quite well with the LS-DYNA prediction till 14 μs (*i.e.*, before the arrival of the second reflection). However, the LS-DYNA solution cannot capture the propagating slow wave modes arriving at around 15 μs as it does not model any coupling between the solid and fluid phase.

To predict the motion of the fluid phase, we can use Eq. 53 to have an estimation of the "Young's modulus" of fluid as well. Thus, for 50 % porosity, E_f is computed at 2.34 GPa for a slow wave speed of 1310 m/s and density of 1960 kg/m^3. For this reduced modulus, the wavelength of the shortest wave is about 0.1 mm. To capture the propagating waves accurately, a mesh of 900,000 elements with element length
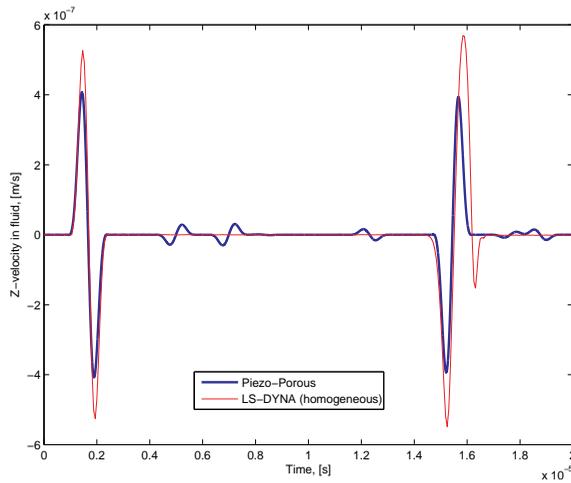
Figure 5: Surface *z*-velocity history in fluid phase as predicted by the present method and LS-DYNA solutions for 50% porosity

of 0.1 mm is generated. The response of this homogenized fluid FE model along with the porous media response is shown in Fig. 5. The figures suggests that a very good agreement of the arrival of the reflected pulse is obtained, although the magnitude of the waves differs by 25 %. Thus, Eq. 53 cannot be used blindly to obtain an equivalent modulus for fluid and an accurate estimation of the equivalent density of fluid should be made first. It is important to note that if the fluid density of 1000 kg/m^3 is used in Eq. 53, then the estimated E_f is 1.2 GPa, which further increases the amplitude of the FE response.

Next the derived fields like strain, stress, electric field and electric displacement are measured at $z = 4.5$ mm (mid-depth) from the surface and compared in Fig. 6. First of all, the strain, stress and electric field histories show multiple reflections occurring at the free and fixed ends of the bone sample. However, the electric displacement generated for the applied mechanical loading is negligible. This is due to relatively smaller values of bone piezoelectric constants compared to the elastic parameters. The first two stress peaks are comparable to the applied stress at the surface. However, the peak values diminish with time. The same observation is true for the strain and electric field envelope. It is interesting to note that the compressive stress and strain are in the same phase (*i.e.*, the peak values are coincident), whereas, the electric field is 180° out of phase to strain (hence, stress).

The advantage of the present formulation is that the response of a porous material to electric pulse can also be investigated. This is taken up next, where the same bone
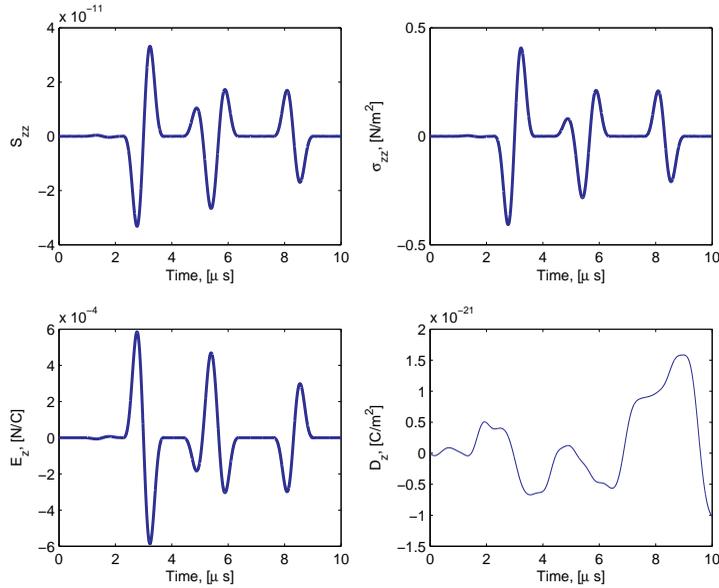
Figure 6: Variation of the strain, stress, electric field and electric displacement measured at the mid-layer of a bone sample for applied mechanical loading on the surface
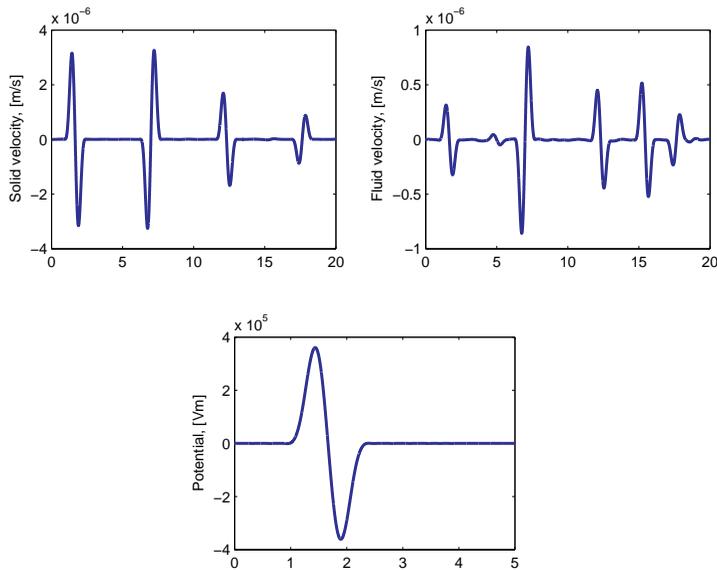

Figure 7: Variation of the solid and fluid velocity and electric potential measured at the surface of a bone sample for applied electrical field on the surface

Parameter	Value	Parameter	Value
e_{31}	6.16 C/m^2	e_{33}	8.34 - j0.251 C/m^2
e_{15}	0.00 C/m^2	$\varepsilon_{11}, \varepsilon_{33}$	4.27 $\times 10^{-9}$ F/m

Table 2: Material properties of PZT considered in this study

model is considered. On the surface of the bone, in the same location an electric pulse is applied in *Z* direction. The temporal and spatial distributions are the same as that of the previously applied mechanical stress. The resulting solid and fluid motion and the electric potential at the surface of the bone sample are shown in Fig. 7. It is worth mentioning that the coupling between solid and fluid induces the fluid-borne wave, even though there is no explicit coupling between the fluid phase and piezo-electricity.

The stress, strain, electric field and electric displacement history for the applied electric displacement at the surface are compared in Fig. 8. The temporal variation of the electric field (E_z) and displacement (D_z) histories at mid-depth are same as that of the original pulse applied at the surface. This indicates the non-propagating nature of the electric field, which can be perceived as a static field (although of different magnitude at different time instances) superposed over the propagating elastic field. The relative magnitude of D_z and E_z is about 10^{-10}, which is close to the value of ε_{33}. This indicates that the D_z envelope does not have sufficient contribution from the mechanical strains. This is partly due to the low magnitude of the induced mechanical strain and low values of the piezoelectric coupling coefficients. The static nature of the electric field is also manifested in the strain history, where the first wave packet appears after 2 μs. This time gap of 1 μs (considering the fact that responses of all other entities appear at 1 μs) can be baffling at first. However, this can be explained by the fact that the displacement field for initial waveform of the electric field is same everywhere resulting in a zero compressive strain ($\partial u_z / \partial z = 0$). Thus, in the beginning, $E_z = D_z / \varepsilon_{33}$, $S_{zz} = 0$ and $\sigma_{zz} = -e_{33} D_z / \varepsilon_{33}$. This also explains the sign and temporal location of the first stress peak (at 1 μs). However, this stress generates solid (and fluid) displacement, which is not constant everywhere and in turn, nonzero compressive strain is produced that arrives after 2 μs. The wave nature of the elastic solid and fluid field generates reflections from the fixed and free end which are further seen in the time history.

4.2   *Response of porous PZT to mechanical loading and electric field*

In the previous example of bone as a porous media, the coupling between elastic and electric field was very poor due to low values of the piezoelectric constant, e_{ij}.
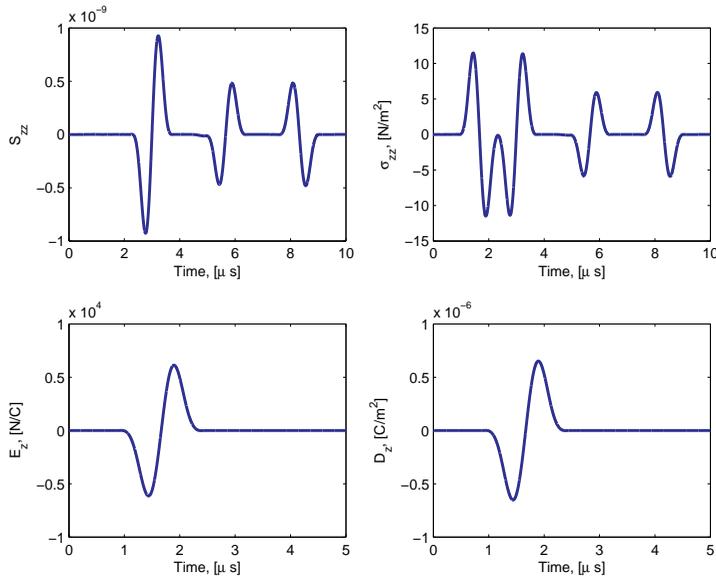
Figure 8: Variation of the strain, stress, electric field and electric displacement measured at the mid-layer of a bone sample for applied electrical field on the surface

However, for porous piezoelectric ceramic materials, e_{ij} (and ε_{ij}) values are quite high (almost 1000 times the bone material constants). Thus, for PZT, greater interaction between the elastic and electric field can be expected. To investigate this feature, a PZT sample of 9 mm thickness is considered and subjected to the same mechanical stress and electric pulse as in the previous example. The material properties of PZT are given in Table 2 where the porosity of the sample is considered as 50 %. To separate out the effect of large electro-mechanical coupling, it is assumed that the solid part of the PZT has the same property as that of bone and the pores of PZT are filled by the same fluid of the previous example.

For applied mechanical stress on the surface, the solid and fluid phase velocity and the electric potential generated at the surface of the sample are shown in Fig. 9. It can be easily seen that the propagation speed of the solid phase in PZT is very high compared to that of bone, as multiple reflections can readily be seen. The attenuation rate of the waveforms is also higher compared to that of bone, which can be attributed to the complex valued e_{33}. Since there is no coupling between the fluid phase and piezo-electricity the slow wave profile is the same as that obtained for bone and no attenuation is visible. On the other hand the electric potential history shows considerable attenuation and wave speeds comparable to the solid-borne wave.
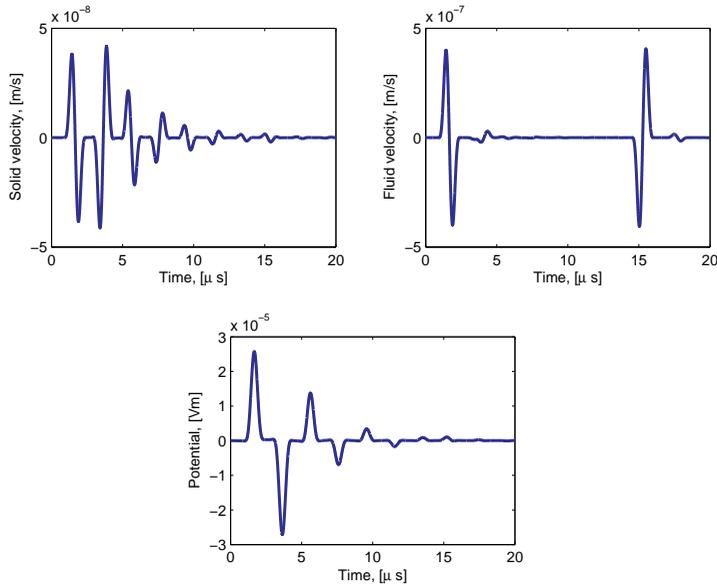
Figure 9: Variation of the solid and fluid velocity and electric potential measured at the surface of a porous PZT sample for applied mechanical stress on the surface
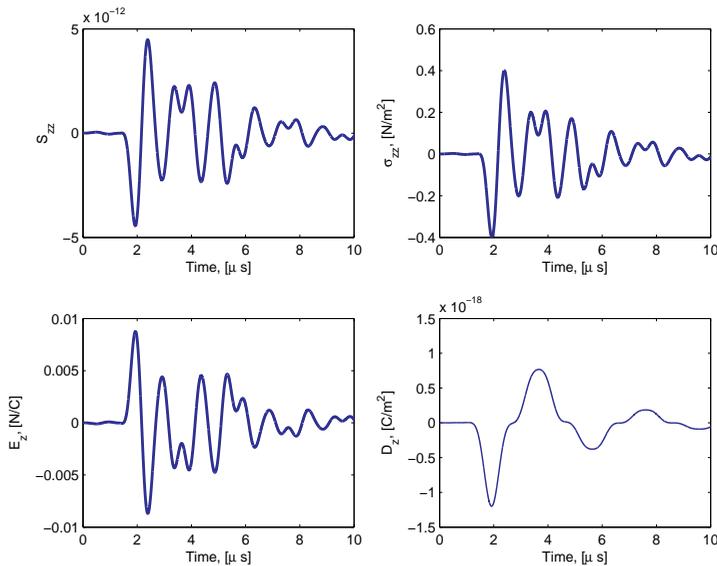

Figure 10: Variation of the strain, stress, electric field and electric displacement measured at the mid-layer of a porous PZT sample for applied mechanical stress on the surface
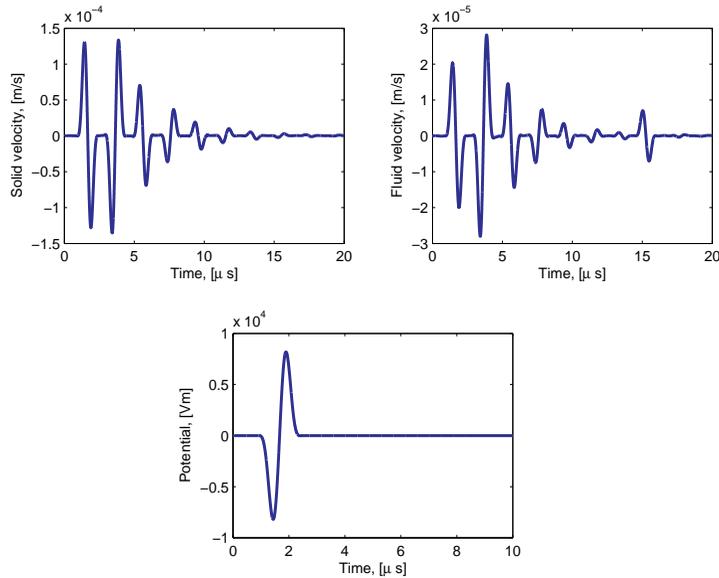
Figure 11: Variation of the solid and fluid velocity and electric potential measured at the surface of a porous PZT sample for applied electric field on the surface

Figure 10 illustrates the strain, stress, electric field and electric displacement measured at the mid-point of the sample. The strain measured in this case is one order lower than that of bone, which is due to piezoelectric stiffening. On the other hand, the magnitude of the electric field is one order higher than the previous case of bone. As observed in the case of bone, the electric displacement generated at the mid-point is negligible. It is interesting to note that the stress/strain waves are much more dispersive compared to the fast and slow waves.

Finally, the same electric field of the previous example is applied on the surface of the porous PZT layer and the surface response is measured and plotted in Fig. 11. The fast wave profile is similar to the previous case of mechanical actuation. However, the slow wave profile is markedly different, in fact, quite similar to the fast wave response. Further, the magnitude of the slow wave mode (appearing at 15 μs) is quite small compared to the mechanically induced wave. These characteristics can be explained by the fact that in the case of electrical actuation, the solid phase is primarily excited, whereas, the fluid phase is excited solely due to the coupling between solid and fluid. Thus, the fluid phase motion is a scaled version of the solid phase motion superposed with the slow wave mode. The input energy is primarily consumed by the solid phase and hence, the reduced peak of the slow wave mode.
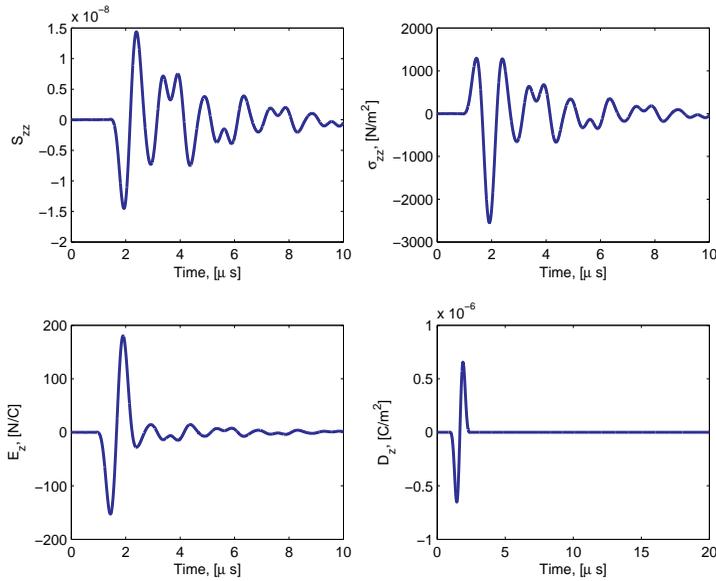
Figure 12: Variation of the strain, stress, electric field and electric displacement measured at the mid-layer of a porous PZT sample for applied electric field on the surface

The strain, stress, electric field and displacement histories at the mid-point of the sample are shown in Fig. 12. It can be observed that the strain wave has finite time gap to reach the mid-point, whereas, the stress and electric field have reached all the points in the domain instantaneously. The reason for this phenomenon is explained in the previous example. Compared to the response of bone (Fig. 8), the electric field history shows many oscillations arising due to the stronger coupling of PZT with the elastic field. The electric displacement field, however, retains its initial shape and static field like characteristic.

5   Summary

A mathematical model of porous piezoelectric media is developed in this work for predicting the response due to dynamic mechanical and electric field. The governing equations of motion are solved in the frequency domain to construct analytical solutions for layered media and half-space. It is assumed that the piezoelectric coupling exists only with the solid phase and the fluid phase is considered inert. The solutions obtained in this work indicate that an application of electric field to a piezoelectric porous material generates both solid and fluid phase deformation.

Further, the electric field generated due to unit mechanical stress in bone is of the order of 0.5 μV/mm. On the other hand for a porous PZT the electric field generated is close to 10 μV/mm. In case of bone, the generated electric field does not show propagating wave behavior and can be thought of as a static field. However, in case of PZT, due to strong coupling, the electric field shows multiple reflections displaying propagating wave behavior. The present model also shows that an applied electric field primarily excites the solid phase of a porous media and the fluid phase is excited due to elastic coupling with the solid phase. Thus, for a mechanical load, the velocity of the fluid phase is more than that of solid phase, whereas, for an electric pulse, the solid phase velocity is more than that of fluid phase. The porous piezoelectric model and the solution strategy presented in this work capture the dynamic behavior of two-dimensional structures at a nominal cost of computation. Future investigation should be directed towards having experimental measurements to validate the present model. The model will also be instrumental in understanding bone regeneration where strong interplay of elastic and electric field exists.

References

Al-Khoury, R.; Kasbergen, C.; Scarpas, A.; Blaauwendraad, J. (2002): Poroelastic spectral element for wave propagation and parameter identification in multi-layer system. *Int. J. Sols. and Str.*, vol. 39, pp. 4073–4091.

Anderson, J.; Eriksson, C. (1970): Piezoelectric properties of dry and wet bone. *Nature*, vol. 227, pp. 491.

Bassett, C.; Becker, R. (1962): Generation of electric potentials by bone in response to mechanical stress. *Science*, vol. 137, pp. 1063.

Biot, M. (1955): Theory of propagation of elastic waves in a fluid-saturated porous solid. I. low-frequency range. *J. Acoust. Soc. Am.*, vol. 28, pp. 168–178.

Braden, M.; Bairstow, A.; Beider, I.; Ritter, B. (1966): Wave propagation modeling in human long bones. *Nature*, vol. 212, pp. 1565–1566.

Bur, A. (1976): Measurements of the dynamic piezoelectric properties of bone as a function of temperature and humidity. *J. Biomechanics*, vol. 1, pp. 495–507.

Chakraborty, A. (2009): Wave propagation in anisotropic poroelastic beam with axial-flexural coupling. *Computational Mechanics*, vol. 43(6), pp. 755–767.

Chakraborty, A.; Gopalakrishnan, S. (2004): A spectrally formulated finite element for wave propagation analysis in layered composite media. *Int. J. Sols. Str.*, vol. 41(18-19), pp. 5155–5183.

Chakraborty, A.; Gopalakrishnan, S. (2004):   Thermoelastic wave propagation in anisotropic layered media: A spectral element formulation. *Int. J. Comp. Meth.*, vol. 1(3), pp. 535–567.

Chakraborty, A.; Gopalakrishnan, S. (2004):   Wave propagation in inhomogeneous layered media: solution of forward and inverse problems. *Acta Mechanica*, vol. 169(1-4), pp. 153–185.

Chakraborty, A.; Gopalakrishnan, S. (2005):   A spectrally formulated plate element for wave propagation analysis in anisotropic material. *Comp. Meth. Appl. Mech. Engg.*, vol. 194(42-44), pp. 4425–4446.

Chakraborty, A.; Gopalakrishnan, S. (2006):   Approximate spectral element fr wave propagation analysis in inhomogeneous layered media. *AIAA Journal*, vol. 44(7), pp. 1676–1685.

Chakraborty, A.; Gopalakrishnan, S. (2006):   A spectral finite element model for wave propagation analysis in laminated composite plate. *J. Vibr. Acoust.*, vol. 128(4), pp. 477–488.

Chakraborty, A.; Gopalakrishnan, S.; Kausel, E. (2005):   Wave propagation in inhomogeneous piezo-composite layer by the thin-layer method. *Int. J. Numer. Meth. Engg.*, vol. 64(5), pp. 567–598.

Degrande, G.; Roeck, G. D. (1992):   A spectral element method for two-dimensional wave propagation in horizontally layered saturated porous media. *Computers & Structures*, vol. 44(4), pp. 712–728.

Dziatkiewicz, G.; Fedelinski, P. (2007):   Dynamic analysis of piezoelectric structures by the dual reciprocity boundary element method. *CMES: Computer Modeling in Engineering and Sciences*, vol. 17(1), pp. 35–46.

Fotiadis, D. I.; Foutsitzi, G.; Massalas, C. (1999):   Wave propagation modeling in human long bones. *Acta Mechanica*, vol. 137, pp. 65–81.

Fukuda, E.; Yasuda, I. (1957):   On the piezoelectric effect of bone. *J. Phys. Soc. Japan*, vol. 12, pp. 1158.

Galassi, C. (2006):   Wave propagation modeling in human long bones. *J. Europe Ceram. Social.*, vol. 26, pp. 2951–2958.

Gjelsavik, A. (1973):   Bone remodeling and piezoelectricity - I. *J. Biomechanics*, vol. 6(1), pp. 69–77.

Gjelsavik, A. (1973): Bone remodeling and piezoelectricity - II. *J. Biomechanics*, vol. 6(2), pp. 187–193.

Gopalakrishnan, S.; Chakraborty, A.; RoyMahapatra, D. (2007): *Spectral Finite Element Method.* Springer.

Han, X.; Ding, H.; Liu, G. R. (2005): Elastic waves in a hybrid multilayered piezoelectric plate. *CMES: Computer Modeling in Engineering and Sciences*, vol. 9(1), pp. 49–56.

Jabbari, E.; Gatmiri, B. (2007): Thermo-poro-elastostatic green's function for unsaturated soils. *CMES: Computer Modeling in Engineering and Sciences*, vol. 18(1), pp. 31–44.

Johnson, D.; Koplik, J.; Dashen, R. (1987): Theory of dynamic permeability and tortuosity in fluid-saturated porous media. *J. Fluid Mech.*, vol. 176, pp. 379–402.

Lakes, R.; Katz, J. (1977): Dielectric relaxation in cortical bone. *J. App. Phys.*, vol. 48, pp. 808–811.

Marino, A.; Becker, R. (1970): Piezoelectric effect and growth control in bone. *Nature*, vol. 228, pp. 473.

Marino, A.; Soderholm, S.; Becker, R. (1971): Origin of the piezoelectric effect in bone. *Calc. Tiss. Res.*, vol. 8, pp. 177.

McElhaney, J. (1967): The charge distribution on the human femur due to load. *J. Bone Joint Surg.*, vol. 49A, pp. 1561.

Mitra, M.; Gopalakrishnan, S. (2006): Wavelet based 2-D spectral finite element formulation for wave propagation analysis in isotropic plates. *CMES: Computer Modeling in Engineering and Sciences*, vol. 15(1), pp. 49–67.

Mitra, M.; Gopalakrishnan, S. (2006): Wavelet based spectral finite element modeling and detection of de-lamination in composite beam. *Proc. Royal Soc. A*, vol. 462(2070), pp. 1721–1740.

Mitra, M.; Gopalakrishnan, S. (2008): Wave characteristics of multi-walled carbon nanotubes. *CMES: Computer Modeling in Engineering and Sciences*, vol. 27(1-2), pp. 125–136.

Park, J.; Kelly, B.; Kenner, G.; Recum, A. (1981): Wave propagation modeling in human long bones. *J. Bio. Mater. Res.*, vol. 15, pp. 103–111.

Reinish, G. (1975):   Piezoelectric properties of bone as functions of moisture content. *Nature*, vol. 253, pp. 626–627.

Seyrafian, S.; Gatmiri, B.; Noorzad, A. (2006):   Green functions for a continuously non-homogeneous saturated media. *CMES: Computer Modeling in Engineering and Sciences*, vol. 15(2), pp. 115–126.

Shamos, M.; Lavine, L.; Shamos, M. (1963):   Piezoelectric effect in bone. *Nature*, vol. 81, pp. 1978.

Tabrez, S.; Mitra, M.; Gopalakrishnan, S. (2007):   Modeling of degraded composite beam due to moisture absorption for wave based detection.   *CMES: Computer Modeling in Engineering and Sciences*, vol. 22(1), pp. 77–89.

Williams, J. (1992):   Ultrasonic wave propagation in cancellous and cortical bone: Prediction of some experimental results by Biot's theory. *J. Acoust. Soc. Am.*, vol. 91(2), pp. 1106–1112.

Wu, K.; Chen, S. (2007):   Two-dimensional dynamic green's functions for piezoelectric material. *CMES: Computer Modeling in Engineering and Sciences*, vol. 20(3), pp. 181–196.

Zhang, H. L.; Li, J.; Zhang, B. (2007):   Wave propagation modeling in human long bones. *Acta Materialia*, vol. 55, pp. 171–181.